Electronic Supplementary Material (ESI) for Nanoscale.

Supporting Information

Memristive Synapse with High Reproducibility for Flexible Neuromorphic Networks Based on Biological Nanocomposites

Jun Ge, Dongyuan Li, Changqiao Huang, Xuanbo Zhao, Jieli Qin, Huanyu Liu, Weiyong Ye, Wenchao Xu, Zhiyu Liu, Shusheng Pan**

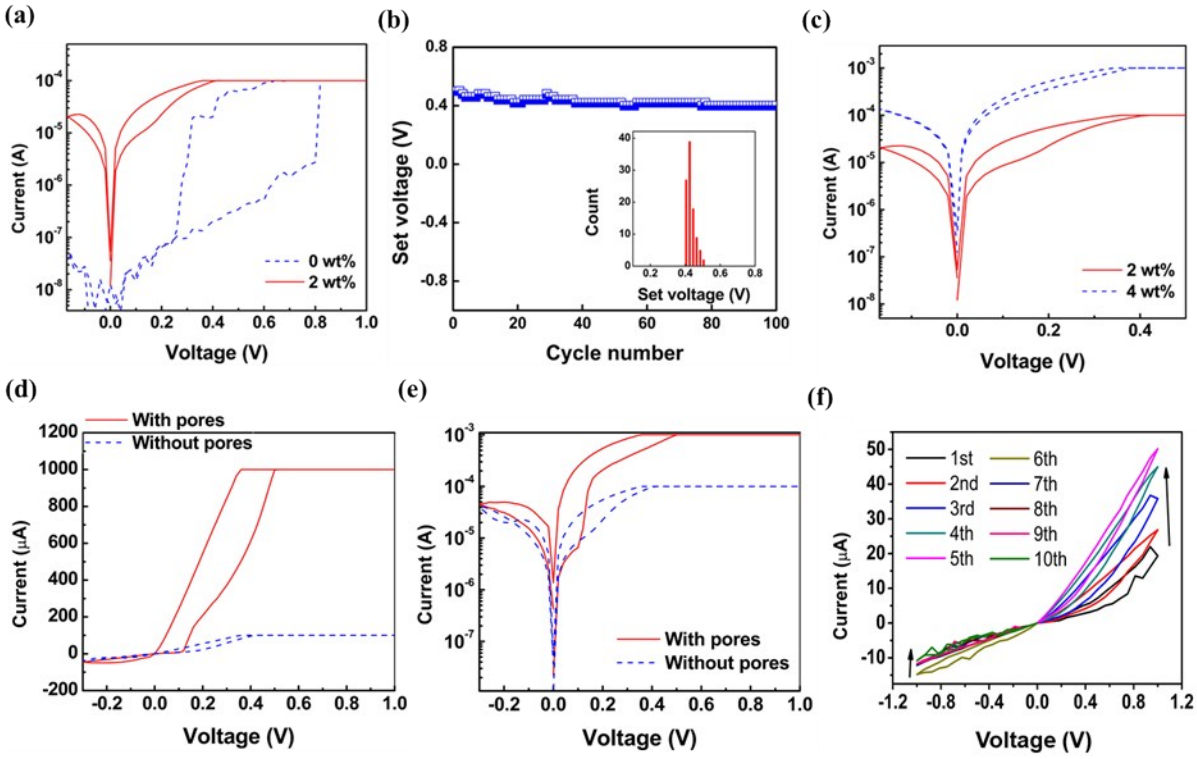

Figure S1. Memristive switching characteristics of different CιC:Ag devices. (a) Measured d.c. I–V characteristics of CιC:Ag device with 0% and 2% Ag doping concentration in the composites. (b) The set voltage variation of the CιC:Ag device over 100 quasi-static I–V sweeps. Inset: histogram for set voltage distribution. (c) Measured d.c. I–V characteristics of devices with 2% and 4% Ag doping concentration. Linear-scale (d) and semilogarithmic (e) d.c. I–V characteristics of CιC:Ag with and without nanopores. (f) Incremental positive and negative I–V sweeps of the NP-CιC:Ag device.

As shown in **Figure S1**a, The Ag/pure-CιC/ITO structured devices show typical volatile threshold switching characteristics (dash line), which is not suitable for artificial synapse applications. In contrast, the current–voltage (I-V) curve of a device with 2 wt% of Ag nanoclusters (relative to CιC) exhibits gradual and nonvolatile RS behaviors (solid line), favoring electronic synapse applications. Moreover, Figure S1b shows that CιC:Ag device demonstrates quite uniform RS with 5.7% temporal set voltage variation (σ/μ) during 100 switching cycles. The above results suggest that the Ag nanoclusters in CιC layer might facilitate and stabilize the

CFs growth through the switching layer, leading to the transition from threshold switching to nonvolatile switching. However, further increasing the amount of Ag dopant to 4 wt% would decrease the on/off ratio of the device, as shown in Figure S1c.

Nanopores result in noticeable changes in the switching characteristics of the devices (Figure S1d and S1e): the on/off current ratio at 0.1 V read voltage increases from ~3 to ~80; the NP-CtC:Ag device can reproducibly operate under a compliance current of 1 mA, which however often lead to irreversible breakdown in pristine CtC:Ag devices. In addition, it is worth mentioning that the NP-CtC:Ag device shows strong rectification characteristics, which may be used to prevent sneak paths in the crossbar array. Figure S1f shows down-up and up-down evolution in current levels during incremental positive 1-5th and negative 6-10th voltage sweeps. The continuously increased and reduced current implies that the memristive device can be potentiated and depressed, well mimicking the behavior of biological synapse.

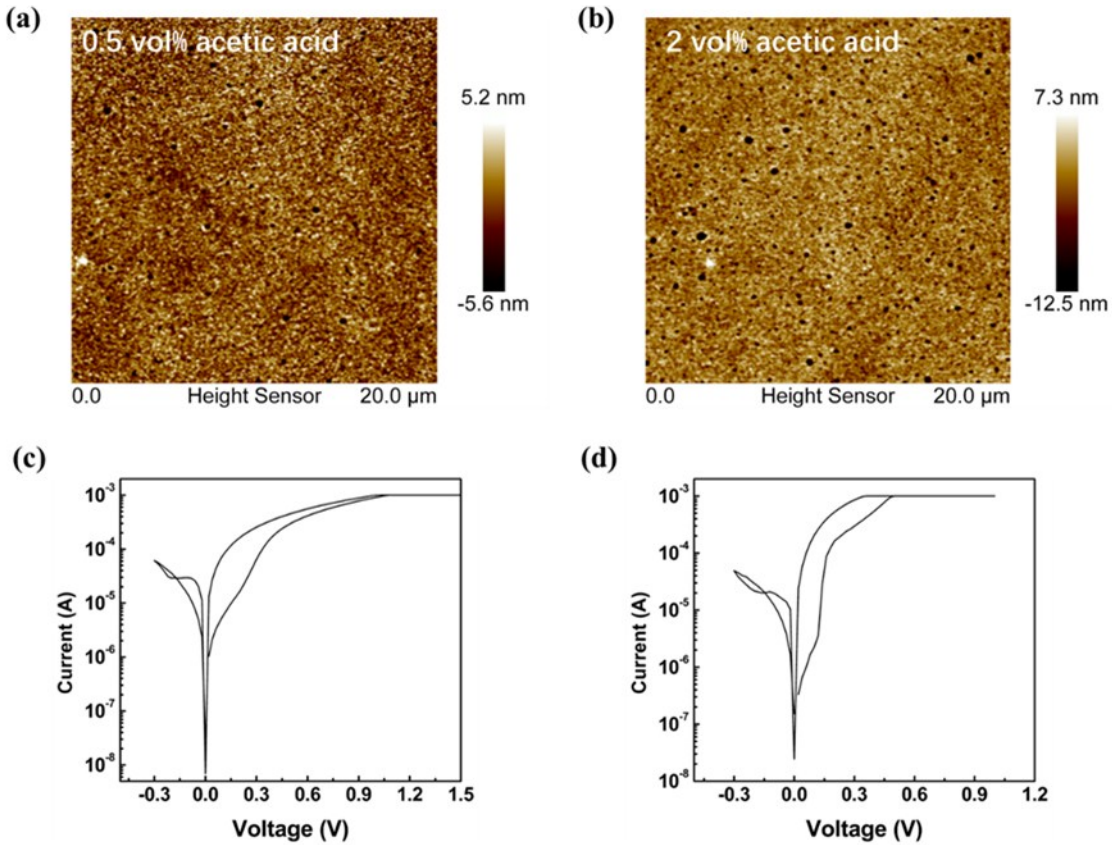

Figure S2. I-V DC sweeps with different acetic acid volume fraction in CιC:Ag 2 wt% solution. (a) an AFM image of a ~80 nm CιC: Ag layer derived from solution with 0.5% volume fraction of acetic acid. The density of nanopores decreases with lower concentration of acetic acid. (b) an AFM image of a ~80 nm CιC: Ag layer derived from solution with 2% volume fraction of acetic acid. (c) I-V DC sweep of a ~80 nm CιC: Ag layer derived from solution with 0.5% volume fraction of acetic acid. The I-V curve shows smaller on/off ratio and larger set voltage. d. I-V DC sweep of a ~80 nm CιC: Ag layer derived from solution with 2% volume fraction of acetic acid. This confirms that nanopores are essential to achieve high performance and adding more content than 1vol% of acetic acid would not severely alter the nanopore density or I-V characteristics of the device.

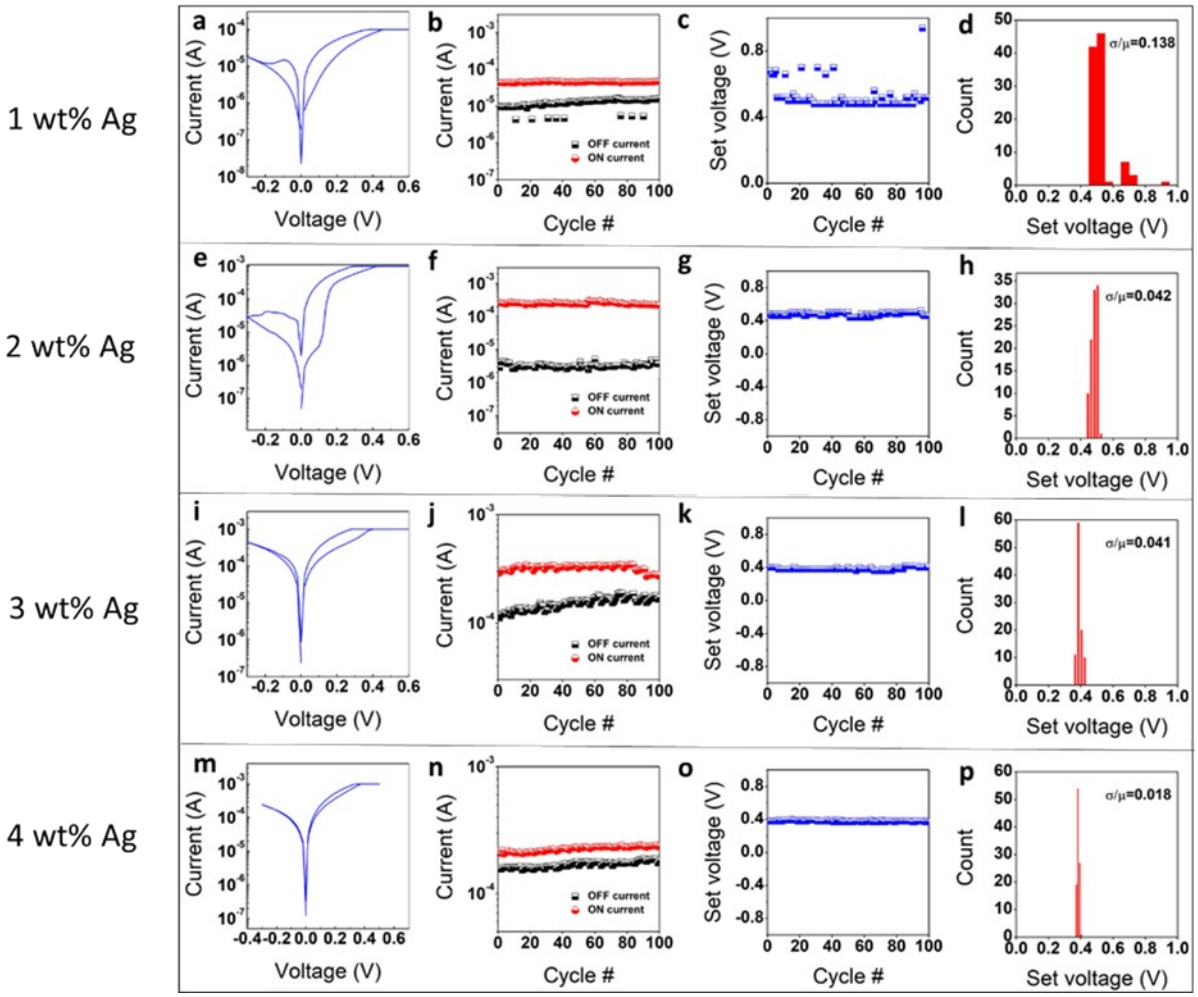

Figure S3. NP-CιC:Ag device performance for different Ag doping levels; 1 wt% (1st row), 2 wt% (2nd row), 3 wt% (3rd row), and 4 wt% (4th row). Shown are DC I-V characteristics, on/off current states at 0.1 V over DC I-V cycles, and set voltage distributions, respectively, for a-d. 1 wt% CιC:Ag, e-h. 2 wt% CιC:Ag, i-l. 3 wt% CιC:Ag, and m-p. 4 wt% CιC:Ag. Ag doping decreases switching variation. However, doping for over 2 wt% results in small on/off ratio due to the high conductance of the device.

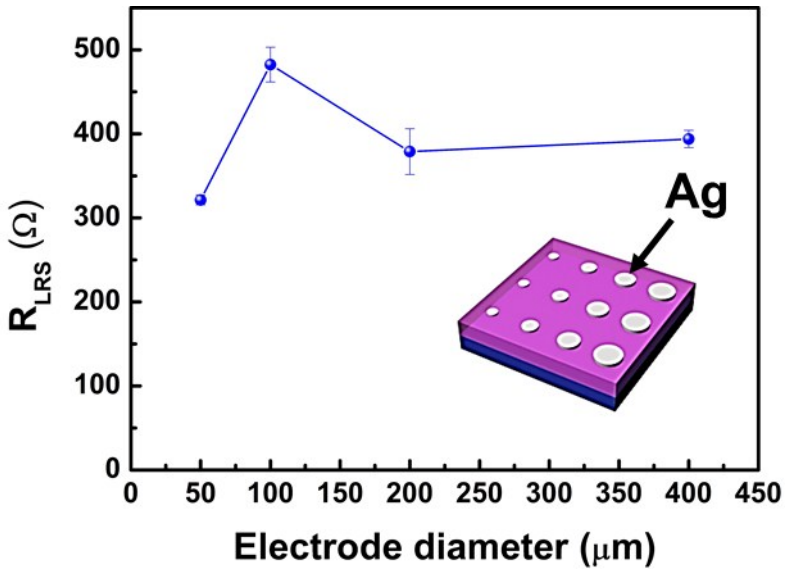

Figure S4. R_{LRS} of Ag/NP-CιC:Ag/ITO versus device size (in diameter) after SET processes (30 SET processes for each device size) under I_{comp} = 1 mA. R_{LRS} shows no dependence on the device electrode area, indicating filamentary nature of LRS.

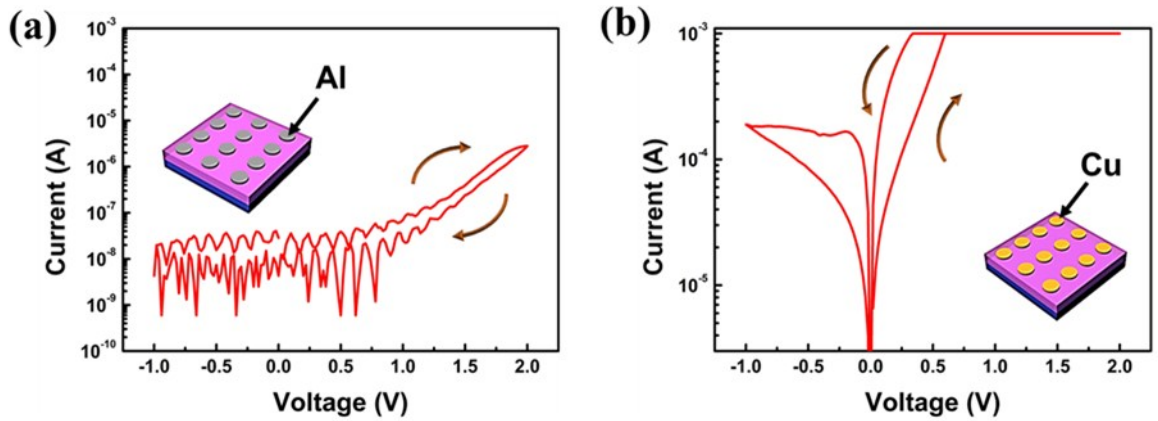

Figure S5. Typical d.c. I–V switching characteristic of the NP-CuC:Ag device using Al electrode (a) and Cu electrode (b). The device exhibits poor resistive switching characteristics with Al electrode. While, the devices with Cu electrode show similar resistive switching characteristics to those with Ag electrode.

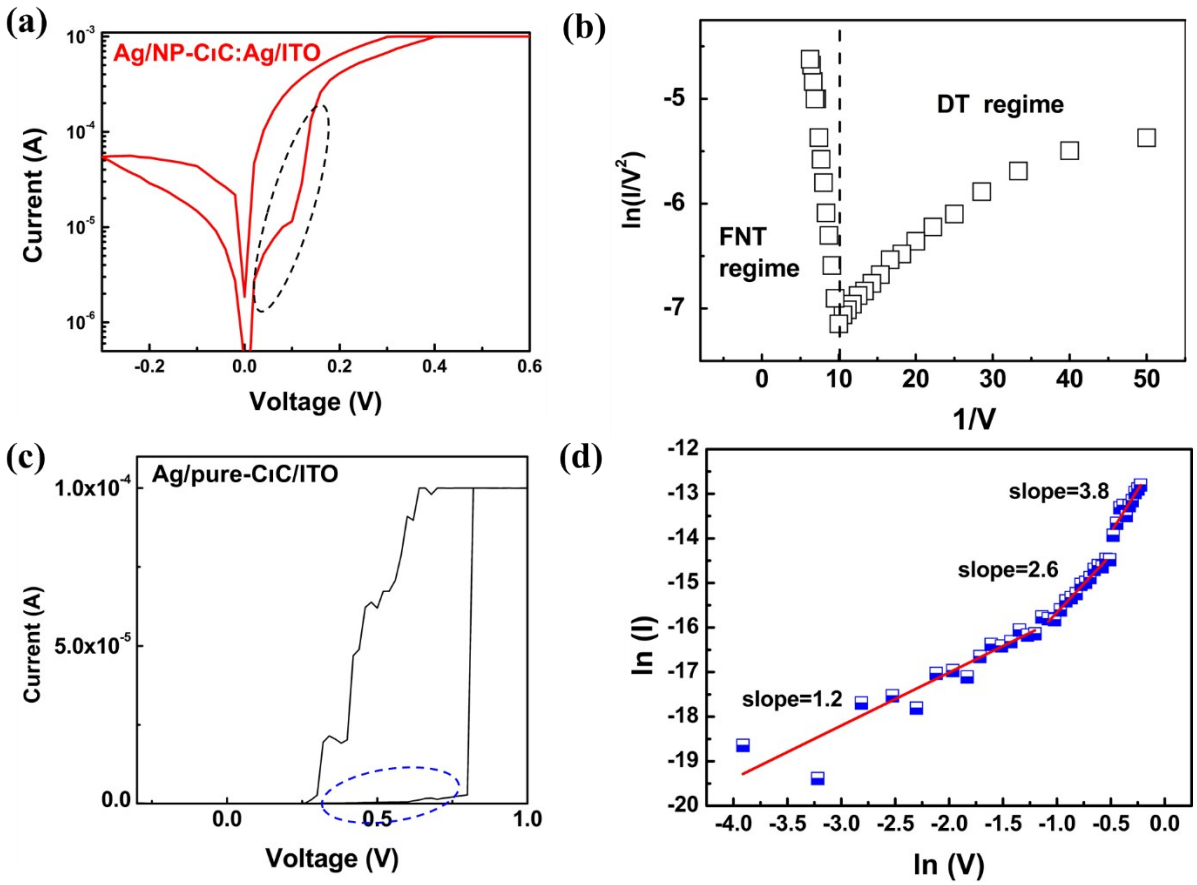

Figure S6. The conduction mechanism analysis of the I-V curve at OFF-states of Ag/NP-CıC:Ag/ITO devices and Ag/pure-CıC/ITO devices. (a) Typical d.c. I–V switching characteristic of the NP-CıC:Ag device using Ag electrode. (b) fitting results of I–V curves of black region in (a). (c) The typical I-V curve of the Ag/pure-CıC/ITO device. (d) The blue region in I-V curves correspond to the SCLC mechanism with three slopes that can be clearly defined with increasing voltage.

We examined conduction mechanisms by fitting I–V characteristics. Specifically, we fit I-V curve data of NP-CıC:Ag device at high resistance state (see Figure S5a): the result was fitted as $\ln(I/V^2)$ versus 1/V, as shown in Figure S5b. The fitting result displays linear behaviors with two parts in the graphs, which correspond to the F–N tunneling conduction model (high voltage region) and directly tunneling (low voltage region), respectively. In contrast, fitting result of Ag/pure-CıC/ITO (Figure S5c and 5d) shows that the charge transport behavior can be well

explained with the trap-controlled space charge limited current classical conduction (SCLC), in which the slope in the HRS region changes from 1.2 to 2.6 to 3.8 with increasing voltage.

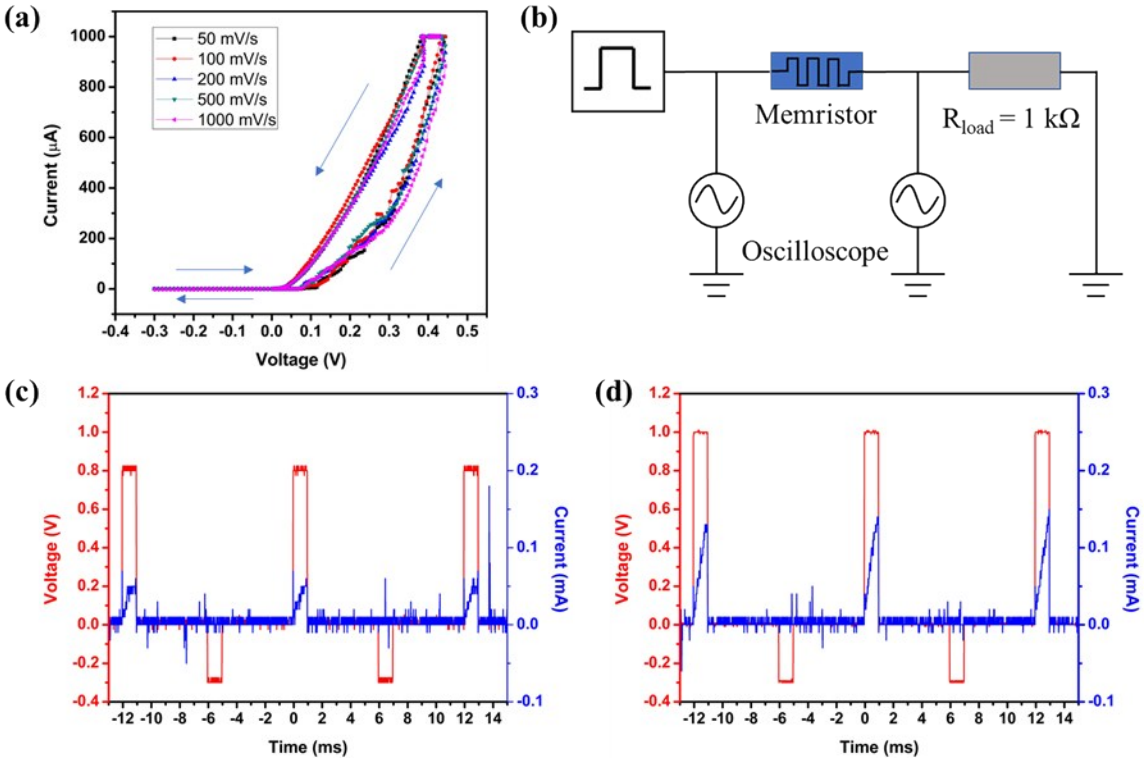

Figure S7. Dynamic properties of the NP-CuC:Ag device. (a) I-V sweep curves at different scan rates; (b) Schematic setup for pulse measurement, which consists of a pulse generator, an oscilloscope, the Ag/NP-CuC:Ag/ITO memory cell, and a load resistor (1 kΩ). (c) (d) Transient responses of the memory in set and reset process with different set voltage amplitudes.

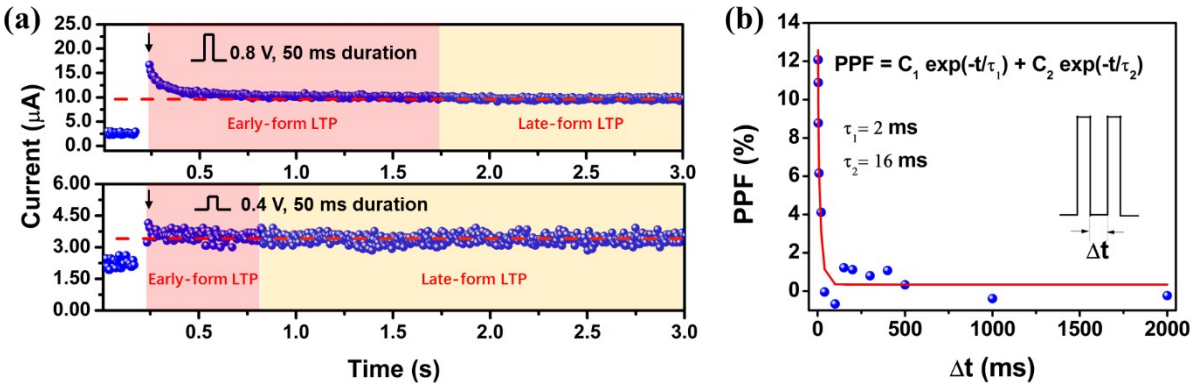

Figure S8. Experimental demonstration of STP, LTP and PPF. (a) EPSCs achieved by presynaptic applied electric pulses. The upper panel shows the ESPC excited by a single electric pulse of 0.8 V while the lower panel records the ESPC excited by a single electric pulse of 0.4 V. The pulse duration is fixed at 50 ms. The device is read at 50 mV. After the first measurement, the device is erased with a negative voltage pulse. (b) Short-term potentiation and paired pulse facilitation. The amount by which the synaptic weight is temporarily modified depends on the time interval between two short 0.3 V pulses. An exponential fit is applied to obtain two characteristic timescales.

In general, EPSC after electrical pulses is used to evaluate the connection strength of the synapse, i.e. the synaptic weight. STP is a temporal change in synaptic weight while LTP corresponds to memory phenomena in biological systems, i.e. the weight change can be maintained for a relatively long time. More specifically, the LTP can be divided into two periods: the fading period in which the memories fade over time, also named as early-form LTP, and the state period in which the synaptic weight remains unchanged, thus the late-form LTP is achieved. Figure S7a shows an example of emulating STP decaying and LTP retaining process in the brain. Strong electrical pulse of 0.8 V induces EPSC to ≈ 17 μA (shown in the upper panel) while the weak electrical pulse of 0.4 V generated EPSC with a magnitude of ≈ 4 μA (shown in the lower panel). The higher level of EPSC indicates a larger weight modulation and the variation of the plasticity is proportional to the amplitude of electrical pulses. Moreover, The EPSC generated by strong

electrical pulse decays to ≈10 μA in ~ 1.8 s and finally stay in the late-form LTP since 2 s. The current level is still 7.5 μA higher than the initial-state current of 2.5 μA before applications of the electrical pulse. In contrast, the memristive synapse applied by a lower 0.4 V electrical pulse exhibits a late-form LTP at a current level of ≈3.7 μA. Therefore, our results fully simulate the synaptic function containing memory decaying and stable periods, and stronger stimulation leads to high level of long-term memory. As an important neuron functionality, paired pulse facilitation (PPF) is also established in NP-CtC:Ag device (Figure. S7b). The PPF exhibits two characteristic timescales, τ_1 = 2 ms and τ_2 = 16 ms, corresponding to the fast and slow decaying terms, respectively.

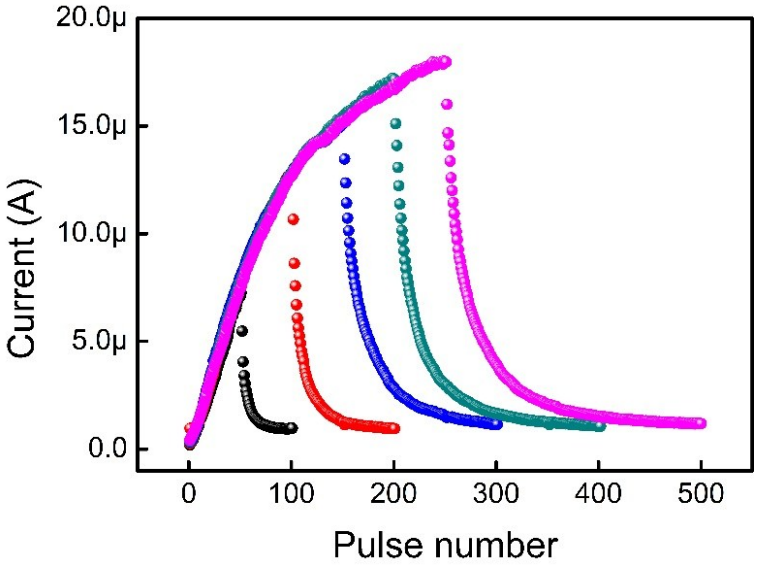

Figure S9. The potentiation and depression characteristics of NP-CιC:Ag memristors with different numbers of state. Potentiation and depression of CιC:Ag by set/reset training pulses showing the maximum analog on/off conductance ratio of ~30. The pulse train consists of consecutive set pulses (1 V, 20 μs) followed by consecutive reset pulses (− 0.5 V, 20 μs). The pulse trains include 50/100/150/200/250 set pulses and 50/100/150/200/250 reset pulses respectively. The current was measured at a 0.1 V read pulse after each set/reset pulse.

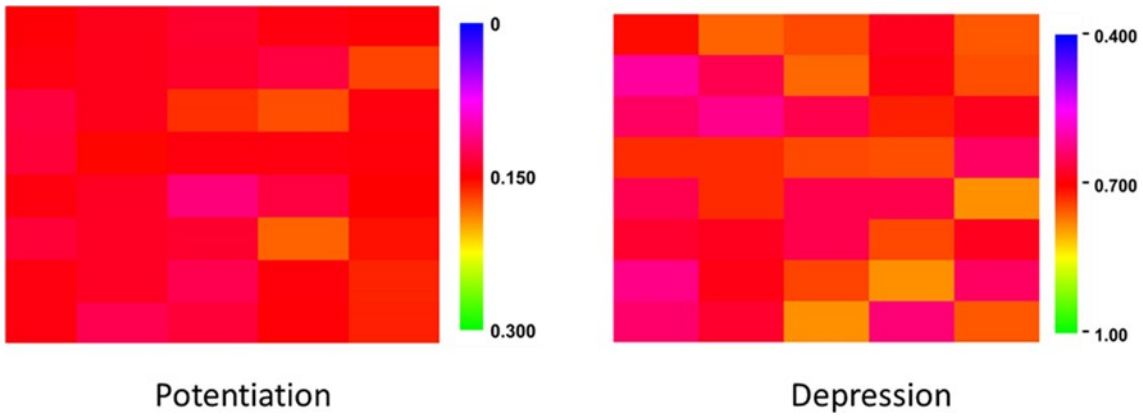

Figure S10. Variation properties of NP-CuC:Ag memristors. Color maps showing spatial variation of linearity for (a) potentiation and (b) depression operations out of 40 cells. The device-to-device variations are 8.84% for potentiation and 7.28% for depression, respectively.

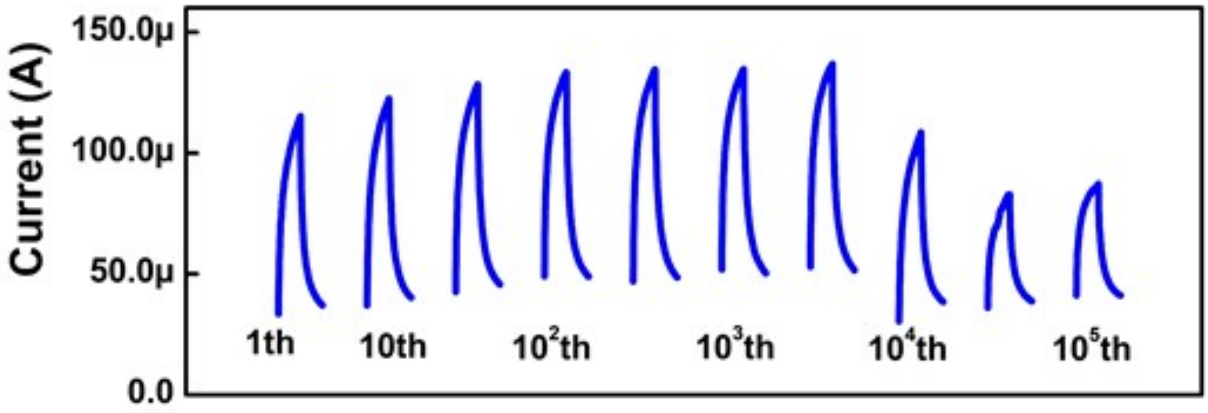

Figure S11. Endurance properties of NP-CuC:Ag memristors. Analog operation can switch for at least 5×10^3 cycles (10^6 set/reset pulses) with a stable switching performance. Each cycle contains 100 set pulses (1 V, 20 μs) and 100 reset pulses (-0.5 V, 20 μs).

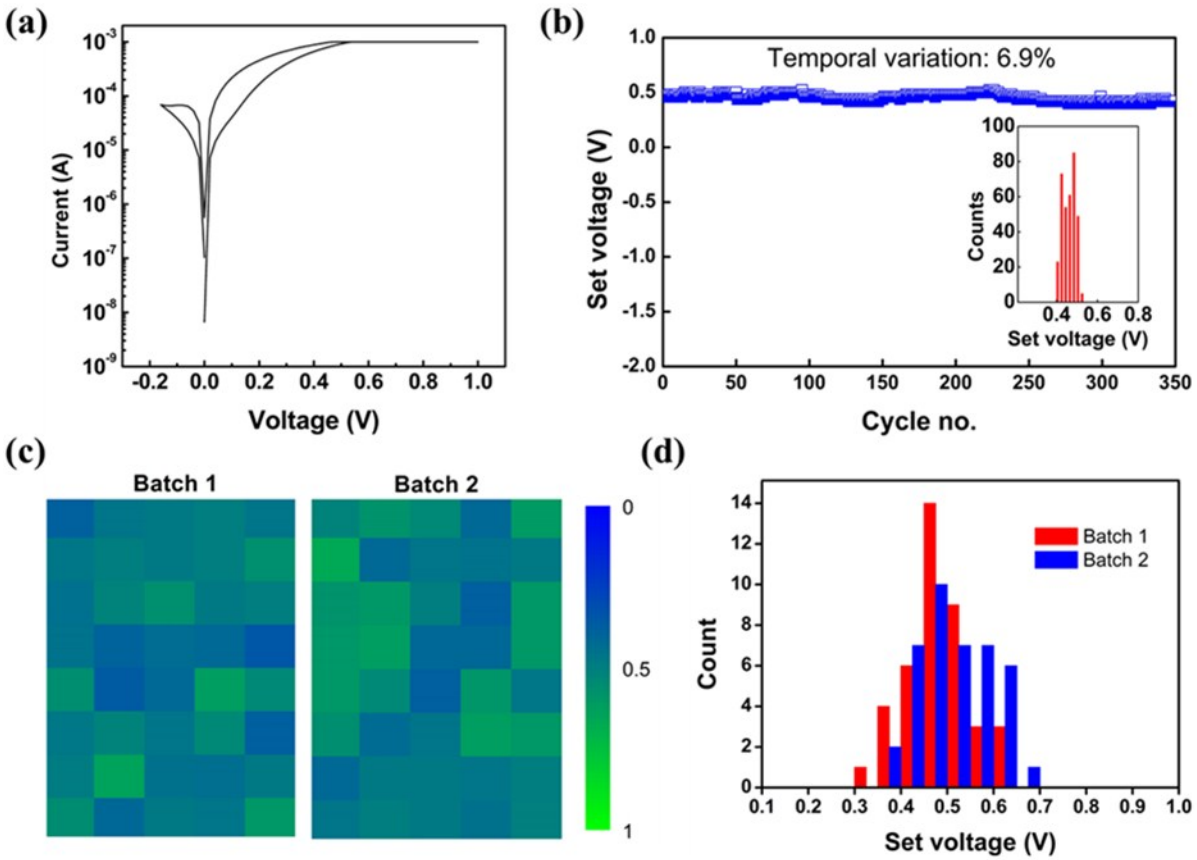

Figure S12. The switching characteristics of flexible NP-CıC:Ag memristive devices. (a) Extracted d.c. I–V switching characteristic of the flexible NP-CıC:Ag device. (b) The temporal set voltage variation of the device over 350 quasi-static I–V sweeps. Insets: the histogram for the set voltage distribution. (c) Map of set voltages of 80 devices (40 devices from batch 1 and 40 devices from batch 2). (d) Histogram for the spatial set voltage distribution shown in (c).

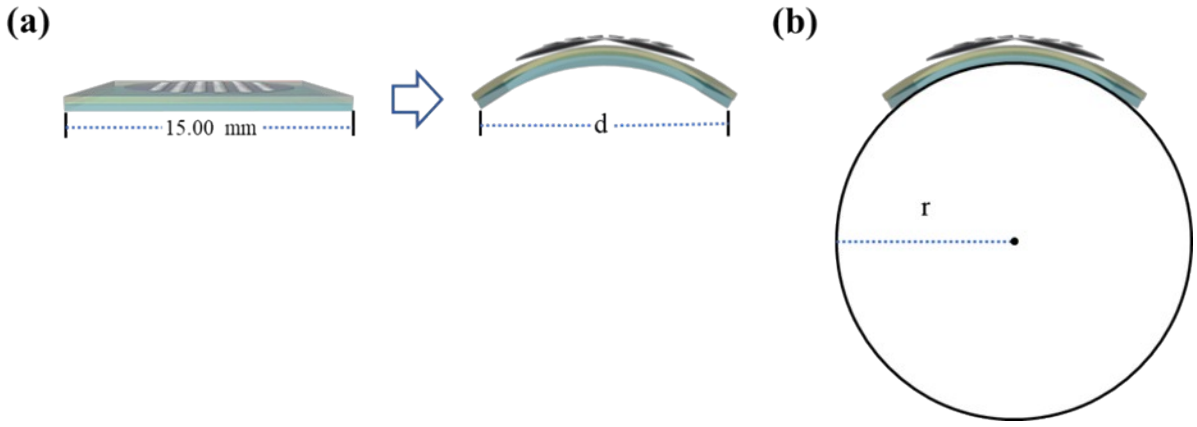

Figure S13. **Schematics of bending tests.** (a) Bending method. (b) Estimation of radius of curvature of the flexile Ag/NP CtC-Ag/ITO memristive device. The strain (%) was calculated from the equation below.

$$\text{Strain (\%)} = \frac{Total\ thickness\ of\ device}{2\ \times radius\ of\ curvature} \times 100$$

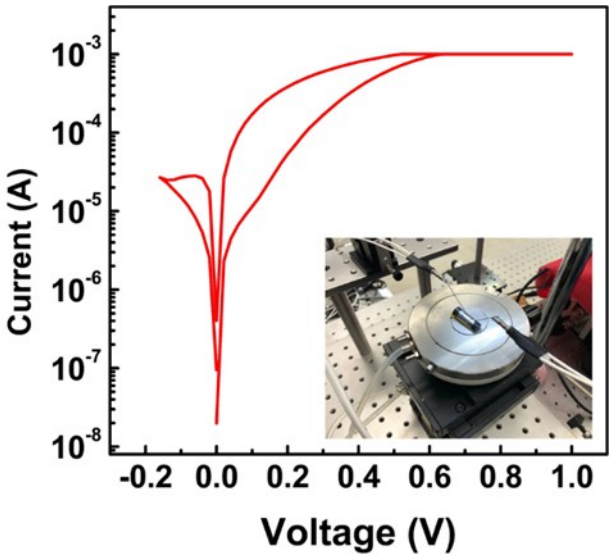

Figure S14. I–V characteristics of Ag/NP CtC-Ag/ITO/PET devices under tensile bending with a radius of curvature of 4.5 mm; inset: photograph of the bent device used for measurement.

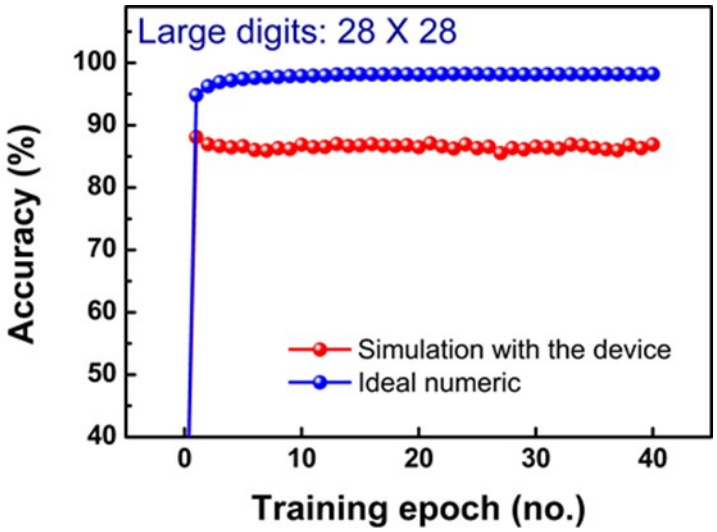

Figure S15. Backpropagation training results using a 28×28 pixel handwritten digit image.